Computer Physics Communications 273 (2022) 108275

Contents lists available at ScienceDirect

Computer Physics Communications

www.elsevier.com/locate/cpc

Double phase transition numerical modeling of superfluid helium for fixed non-uniform grids ☆

Andrea Vitrano *,[1], Bertrand Baudouy

Université Paris-Saclay, CEA, Département des Accélérateurs, de la Cryogénie et du Magnétisme, Gif-sur-Yvette, 91191, Essonne, France

ARTICLE INFO

Article history:
Received 26 August 2021
Received in revised form 1 December 2021
Accepted 20 December 2021
Available online 28 December 2021

Keywords:
Superfluid helium
Phase transition
Finite volume method
Multiphase
Fixed grid
Heat transfer

ABSTRACT

A thermo-fluid dynamic numerical model for the simulation of the first-order and second-order phase transitions in superfluid helium (He II) is presented. The model is based on a Finite Volume Method algorithm for transient multidimensional problems. The method is also intended to simulate the conjugate heat transfer between helium and solids, which required the implementation of customized boundary conditions to replicate the Kapitza resistance and superfluid partial slip. The implemented governing equations for He II constitute an advanced version of an existing single-fluid model, which is herein newly derived with a more generalized conductive heat power law. The vapor-He I phase change is addressed through an explicit calculation of the volume fractions of the helium mixture and by introducing surface tension forces. An algorithm for fixed non-uniform orthogonal grids is conceptualized to deal with the lambda transition. The model is validated against data collected during clamped heat flux experiments in a rectangular cross-section channel of a high aspect ratio. The experiments were conducted both above and below the lambda temperature at atmospheric pressure with the channel in horizontal and vertical positions. The comparison with the data showed satisfactory agreement in the temperature profiles.

1. Introduction

Particle accelerators play a central role in the advancement of fundamental physics research. In circular accelerators such as the Large Hadron Collider (LHC) at CERN, the trajectory of the particle beams must be bent with magnetic fields. For this purpose, the LHC utilizes superconducting dipole magnets. A cooling system of superfluid helium (He II) ensures the superconducting state by maintaining the magnets at temperatures below 2 K [1]. However, the confined structures surrounding the dipole coils hinder the cooling process [2]. If the magnets lose the superconductive properties during a magnet quench, the energy dissipated is such that helium undergoes drastic thermodynamic changes. Being able to simulate numerically these phenomena is then important for the proper design of a magnet and its protection.

He II is used as a thermal vector because of its extraordinary heat extraction capability. The thermal conductivity of He II depends strongly on the magnitude of heat currents potentially present. In the heat flux range of magnet cooling applications, the He II thermal conductivity is even larger than the one of metals, being then several orders of magnitude higher than for He I. The one-dimensional steady-state heat transport in He II is determined by

$$\frac{\mathrm{d}T}{\mathrm{d}x} = -f(T,p)q^n, \tag{1}$$

where T is the temperature, q is the heat flux, and $f(T,p)$ is known as heat conductivity function. The coefficient n depends on the temperature and ranges from 3 to about 4 around T_λ [3–5]. Some authors used 3.4, which is a good approximation in the range of temperatures between 1.7 K and T_λ [6]. In particular, Sato et al. performed a series of experiments at steady-state conditions to derive an accurate correlation for the heat conductivity function for $n = 3.4$ [7].

The present work focuses on the numerical modeling of the double phase transition occurring in He II when subjected to heat flux higher than the critical value at atmospheric pressure. Above this critical heat flux (lambda heat flux) 'colored at atmospheric pressure, He II undergoes the so-called λ-transition and turns into normal subcooled liquid helium (He I) [8]. If the heat flux is also higher than the peak nucleate boiling value, He I vaporizes and

☆ The review of this paper was arranged by Prof. Blum Volker.

* Corresponding author.
E-mail address: andrea.vitrano@cern.ch (A. Vitrano).
[1] Also at CERN, Meyrin, 1211, Switzerland.

https://doi.org/10.1016/j.cpc.2021.108275

forms a helium vapor film that blankets the heating surface. Since the peak nucleate boiling heat flux is significantly lower than the lambda heat flux, if He II undergoes λ-transition the heat flux is large enough to trigger the He I-vapor phase change too [8], resulting in a stable triple-phase phenomenon [9,10].

The λ-transition is characterized by the absence of latent heat of vaporization and a discontinuity of certain thermophysical properties such as the specific heat capacity. As such, the He II-He I phase change is a second-order phase transition according to the Ehrenfest classification [11]. This classification associates each transition type with a specific order, which is determined by the lowest derivative of the Gibbs free energy that shows a discontinuity at the transition point. Since entropy is a first-order derivative of the Gibbs free energy, first-order transitions exhibit an entropy discontinuity, which implies the presence of latent heat. It follows that the He I-vapor phase change belongs to this category. On the other hand, second-order transitions are not isothermal processes and the temperature dependence of entropy is continuous, like in the case of the λ-transition. These types of transitions are discontinuous in the specific heat, which is a second-order derivative of the Gibbs free energy. At atmospheric pressure, the second-order and first-order transitions occur respectively at around 2.17 K (λ-point) and 4.2 K (saturation point). Some thermophysical properties vary substantially across the λ-transition. For instance, the specific heat of helium at the λ-point is more than seven times higher than at 2.2 K [8].

The numerical modeling of the helium phase transitions in multidimensional domains is a rarely approached subject in scientific research. The variations of several orders of magnitude in the thermophysical properties between the different phases of helium represent a severe obstacle for the convergence stability of numerical simulations. For this reason, not many sources with regards to this topic can be found in the literature. Some authors attempted at simulating one or both phase transitions with different assumptions to simplify the problem. Hama and Shiotsu constructed a two-dimensional model to simulate film boiling on a vertical plate [12]. They assumed the solid surface temperature as uniform, negligible thickness of the vapor film, and steady convection mechanism in the vapor phase. Noda et al. developed a one-dimensional model for forced flow applications using empirical formulae for the friction force and zero heat conduction in the two-phase region (He I-vapor mixture) [13]. Okamura et al. developed a two-dimensional finite element model to simulate the λ-transition in natural convection [14]. The models implementing also conjugate heat transfer with solids are even scarcer. Mao et al. utilized an adaptive mesh algorithm to resolve the λ-front in one-dimensional cable-in-conduit conductors [15]. They neglected convection effects, gravity, He I heat conduction, and solid heat conduction in the He II region.

In the present work, both the second-order and first-order phase transitions are dealt with. Due to the peculiar characteristics of superfluid helium, it was decided to utilize as a base solver the open-source C++ toolbox OpenFOAM® [16], which ensures versatility and freedom to modify the existing modules in order to overcome the difficulties imposed by He II physics. The present solver, which for simplicity will be addressed as *heliumChtFoam* from now on, is based on the Finite Volume Method (FVM) and is capable of simulating the helium-solid thermal interaction via a conjugate heat transfer algorithm. Taking into account the complexity associated with a double phase transition, it was decided to partly simplify the problem by considering orthogonal grids only. Moreover, as the intention is to carry out simulations in multi-dimensions, the solution algorithm is designed for fixed non-uniform grids in order to avoid the extra computational time that an adaptive mesh code would require to refine high gradient areas.

2. He II single-fluid model

He II can be thought of as a mixture of two fluid components: a normal component that behaves like a classical viscous fluid and carries all the thermal energy; a superfluid component that has no entropy and no viscosity [17]. Each of them is associated with a velocity that is independent of the other. The normal fluid is characterized by the density ρ_n and the superfluid by ρ_s, which are related to the total density ρ of the liquid by

$$\rho = \rho_n + \rho_s. \tag{2}$$

The mass flux density of He II thus can be expressed as

$$\rho \mathbf{v} = \rho_n \mathbf{v}_n + \rho_s \mathbf{v}_s, \tag{3}$$

where $\mathbf{v}_n$ and $\mathbf{v}_s$ are the velocities of the normal and superfluid components respectively. As the normal component is the energy carrier of He II, the conductive heat flux q in Eq. (1) is equal to

$$\mathbf{q} = \rho s T \mathbf{v}_n = \rho_s s T \mathbf{v}_{ns}, \tag{4}$$

where s is the specific entropy and $\mathbf{v}_{ns}$ is the relative velocity between the fluid components. Because of the two-motion nature of He II, a zero net mass flow does not imply that the fluid is static. Instead, from Eq. (3) follows that the two components can still flow in opposite directions giving rise to an internal convection known as counterflow. The counterflow mechanism contributes to the thermo-mechanical effect — a phenomenon for which establishing a temperature gradient in He II causes a pressure difference and vice versa [18]. If the relative velocity $\mathbf{v}_{ns}$ is below a certain critical value (i.e., very low heat flux), the fluid mechanics of He II is well represented by Landau's two-fluid model [19], which comprises one momentum equation per fluid component. Above the critical value, quantum vortices arise in the fluid and the superfluid component enters the turbulent regime [20]. The quantum turbulence is caused by a viscous-like mechanism between the superfluid and normal components of He II. This mechanism produces a force called mutual friction force [21]. Since the mutual friction force affects significantly the thermo-fluid dynamics of He II, it is necessary to include it in the two-fluid model to come up with a general system of equations that characterizes He II macroscopically. This system is constituted by the Hall-Vinen–Bekharevich–Khalatnikov (HVBK) equations [22,23]. The HVBK equations can be considered as a generalization of Landau's two-fluid model involving also quantum turbulence.

Various authors used numerical methods to obtain steady-state and transient solutions of the HVBK equations for different problems [24–27]. However, the numerical solution of a set of governing equations that includes two momentum equations may result in high computational time depending on the size of the mesh. If a pressure-correction method is used, the complexity of the model increases even further because of the need to modify the segregated algorithm [28]. Since this work aims at multidimensional simulations, it was decided to simplify the two-fluid model to obtain a single-fluid momentum equation that considers He II as a whole fluid. Over the years, some authors faced the problem with a similar approach. Kashani et al. modified the energy equation to take the counterflow into account in one-dimensional forced flow problems [29]. Ramadan and Witt derived a total fluid equation for natural convection problems by neglecting the thermo-mechanical and mutual friction terms, the effect of which was included in the energy equation [30]. Bottura and Rosso derived a set of one-dimensional compressible equations for He II in terms of primitive variables instead of conserved quantities [31]. Kitamura et al. found a way to neglect the superfluid momentum equation by including additional terms in the total fluid equation [32]. In this work, the latter approach is adopted and modified.

For sufficiently high heat fluxes (i.e., engineering applications of He II), the superfluid dynamics is largely determined by the mutual friction force and thermo-mechanical effect, which prevail over the other terms by several orders of magnitude [32]. Similarly to what was done by Kitamura et al., the superfluid component momentum equation can be simplified then to

$$A_{GM}\rho_n \mathbf{v}_{ns}^n = -s\nabla T, \tag{5}$$

where the LHS and RHS are the mutual friction force and thermo-mechanical term respectively; A_{GM} is the Gorter-Mellink coefficient, a He II property that depends on the temperature as $A_{GM} \propto T^3$. Eq. (5) can be rearranged into

$$\mathbf{v}_{ns} = -\left(\frac{s}{A_{GM}\rho_n \|\nabla T\|^{n-1}}\right)^{\frac{1}{n}} \nabla T, \tag{6}$$

where the temperature gradient has been linearized. We can relate $\mathbf{v}_s$ to $\mathbf{v}_{ns}$ and $\mathbf{v}$ through Eq. (3) and the definition of $\mathbf{v}_{ns}$:

$$\mathbf{v}_s = \mathbf{v} - \frac{\rho_n}{\rho}\mathbf{v}_{ns}. \tag{7}$$

Substituting Eq. (6) into Eq. (7) yields

$$\mathbf{v}_s = \mathbf{v} + \left(\frac{s\rho_n^{n-1}}{A_{GM}\rho^n \|\nabla T\|^{n-1}}\right)^{\frac{1}{n}} \nabla T. \tag{8}$$

Similarly, for $\mathbf{v}_n$:

$$\mathbf{v}_n = \mathbf{v} - \left(\frac{s\rho_s^n}{A_{GM}\rho^n\rho_n \|\nabla T\|^{n-1}}\right)^{\frac{1}{n}} \nabla T. \tag{9}$$

Let us write the total fluid momentum equation in its compressible form:

$$\begin{aligned}&\frac{\partial}{\partial t}(\rho_n\mathbf{v}_n + \rho_s\mathbf{v}_s) + \nabla\cdot(\rho_n\mathbf{v}_n\otimes\mathbf{v}_n + \rho_s\mathbf{v}_s\otimes\mathbf{v}_s)\\ &= \mu\left[\nabla^2\mathbf{v}_n + \frac{1}{3}\nabla(\nabla\cdot\mathbf{v}_n)\right] - \nabla p + \rho\mathbf{g},\end{aligned} \tag{10}$$

where t is time, p is the pressure, $\mathbf{g}$ is the gravitational acceleration, and μ is the dynamic viscosity. By substituting Eqs. (8) and (9) into Eq. (10) and rearranging we obtain

$$\begin{aligned}\frac{\partial}{\partial t}(\rho\mathbf{v}) = &-\nabla\cdot(\rho\mathbf{v}\otimes\mathbf{v}) + \mu\left[\nabla^2\mathbf{v} + \frac{1}{3}\nabla(\nabla\cdot\mathbf{v})\right] - \nabla p + \rho\mathbf{g}\\ &- \frac{\mu\rho_s}{\rho}M\left[\nabla^2(\nabla T) + \frac{1}{3}\nabla\left(\nabla^2 T\right)\right]\\ &- \nabla\cdot\left[\frac{\rho_n\rho_s}{\rho}M^2\nabla T\otimes\nabla T\right],\end{aligned} \tag{11}$$

where

$$M \equiv \left(\frac{s}{A_{GM}\rho_n \|\nabla T\|^{n-1}}\right)^{\frac{1}{n}}, \tag{12}$$

which may be considered as a momentum diffusivity per unit of temperature increase. As such, it is a measure of the rate of the mass transfer due to a temperature gradient. Under the assumption (5), Eq. (11) has the great advantage of modeling He II fluid dynamics without taking into account singularly the velocity field of each fluid component. This is achieved because of the last two terms on the RHS of Eq. (11), which are additional contributions to the ordinary Navier-Stokes equations. Since these two additional terms are not velocity dependent, they are computed explicitly by taking the temperature field of the previous time step.

A complete set of governing equations requires also the equations of continuity and energy. The continuity equation can be written as

$$\frac{\partial\rho}{\partial t} + \nabla\cdot(\rho\mathbf{v}) = 0. \tag{13}$$

The energy equation can be expressed in terms of the enthalpy as [33]

$$\begin{aligned}&\frac{\partial}{\partial t}(\rho h) + \nabla\cdot(\rho\mathbf{v}h) + \frac{\partial}{\partial t}(\rho K) + \nabla\cdot(\rho\mathbf{v}K)\\ &= \frac{\partial p}{\partial t} - \nabla\cdot\mathbf{q} + \rho\mathbf{v}\cdot\mathbf{g},\end{aligned} \tag{14}$$

where h is the specific enthalpy and K is the kinetic energy. Combining Eq. (4) with Eq. (6) and substituting the temperature gradient with the enthalpy gradient provides an expression for the heat flux $\mathbf{q}$ in Eq. (14):

$$\mathbf{q} = \frac{k_{eff}}{c_p}\nabla h, \tag{15}$$

where the pressure dependence of the thermophysical properties has been neglected. The latter assumption is justified by the case studies of this research, that is, heat driven phase change phenomena associated with low pressure variations. The property k_{eff} can be considered as the effective thermal conductivity of He II and reads

$$k_{eff} \equiv \left(\frac{1}{f(T,p)\|\nabla T\|^{n-1}}\right)^{\frac{1}{n}}, \tag{16}$$

where the heat conductivity function is computed with Sato's empirical function [7].

Eqs. (13), (11), and (14) constitute the set of single-fluid governing equations of *heliumChtFoam*. This set of equations differs from Kitamura's one essentially in the value of n, in its use, and in the variable of the energy equation. In the derivation of their model, Kitamura et al. set $n = 3$ in the main assumption (Eq. (5)), as this is the value that emerges from the theoretical formulation of the two-fluid model. However, as explained in Section 1, the value of n varies according to the temperature. It is worth observing that the condition $n \neq 3$ has been applied in the past to the He II heat transport but never to the fluid transport [4–6]. Nevertheless, the exponent n originates from the mutual friction term in the superfluid momentum equation and, as such, it must influence the fluid transport too. Therefore, in this work, the derivation of the single-fluid equations has been generalized for an arbitrary exponent n, whose usage has been extended to the momentum equation as well as the energy equation. Moreover, the energy equation has been formulated in terms of a state function in place of the temperature. The latter modification represents a benefit in terms of numerical treatment of the first-order phase transition, as will be clear in the next section.

3. Phase change modeling

The He II model just presented must be modified to include helium multiphase phenomena. In this section, modifications and additional modules due to the second-order and first-order phase transitions are presented.

3.1. Second-order phase transition

As described in Sec. 1, the phase transition between He II and He I is of second-order and hence it is not associated with latent heat. Therefore, the change from one phase to the other occurs instantaneously once T_λ is reached. The superfluid volume fraction

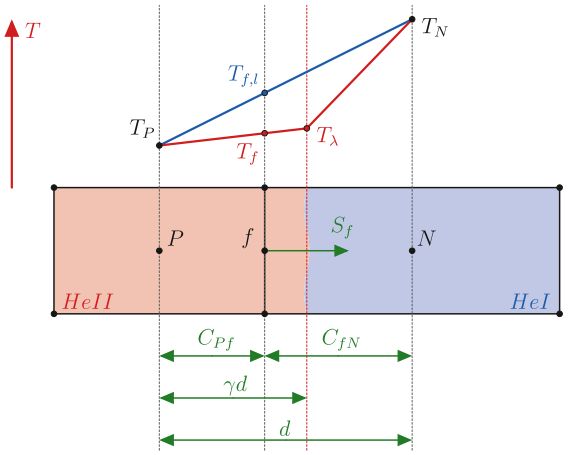

Fig. 1. Schematic representation of the lambda front in two adjacent control volumes of a two-dimensional non-uniform grid.

α_{II}, thus, takes the form of a Boolean parameter that defines exactly the presence of either He II or another phase. Moreover, since the density is continuous across the λ-transition [8], no additional tension force is required at the interface. The critical subject about the λ-transition pertains, instead, to the discontinuity of the specific heat and thermal conductivity at the λ-point. In this subsection, a novel algorithm designed to face this issue in fixed grids is formulated and discussed. The algorithm is constructed specifically for the FVM, in alignment with the structure of *heliumChtFoam*. In the FVM, the computational domain is subdivided into a predefined number of cells called control volumes that constitute the computational grid. Each control volume is characterized by a centroid and a finite number of bounding faces that define the shape of the cell. The centroids of the control volumes coincide with the computational locations where the governing equations are solved for the variables.

3.1.1. Effective thermal conductivity correction algorithm

As seen in Sec. 2, the effective thermal conductivity of He II k_{eff} depends also on the temperature gradient (see Eq. (16)). This dependency is valid as long as the local temperature is below the λ-point. If the second-order phase transition occurs though, a front separating the two phases appears in the computational domain. Due to the considerable difference in the thermal conductivity between the two phases, the temperature gradient changes drastically at the location of the λ-front. The gradient calculation in the mesh cells located across the front carries an intrinsic error due to the way the gradient is numerically approximated. The source of the error can be identified with the linear interpolation of the temperature at the face separating the cells, which will be described later in this section. In this case, a correction of k_{eff} is needed to take into account this error.

The approach presented here is based on the interfacial heat transfer between He I and He II at the λ-front. The main goal is to identify the actual location of the front in order to correct the temperature gradient field and consequently k_{eff}. As a reference for the equations, let us consider the case displayed in Fig. 1, in which the λ-front is situated in an arbitrary location between the centers of two adjacent cells in the computational domain. The first step is to define the heat flux q_{II} through the He II phase from Eq. (1):

$$q_{II} = -\left(\frac{1}{f(T,p)}\frac{T_\lambda - T_P}{\gamma \|\mathbf{d}\|}\right)^{\frac{1}{n}}, \tag{17}$$

where $\mathbf{d}$ is the distance vector between the two cell centers, T_λ is the temperature at the λ-point, and γ is a coefficient whose value is between 0 and 1. The subscript P refers to the centroid of the owner cell, from which the surface normal vector ($\mathbf{S}_f$ in Fig. 1) points outward. From the point of view of the neighbor cell with centroid N, $\mathbf{S}_f$ will then point inward. Let us consider a fictitious heat flux $q_{II,fict}$ between the cell centers that does not take into account the change in temperature steepness across the front like it would be computed without correction:

$$q_{II,fict} = -\left(\frac{1}{f(T,p)}\frac{T_N - T_P}{\|\mathbf{d}\|}\right)^{\frac{1}{n}}, \tag{18}$$

where the subscript N refers to the center of the neighbor cell. The heat flux q_{II} can be expressed as a function of $q_{II,fict}$:

$$q_{II} = \gamma^{-\frac{1}{n}} q_{II,fict}\left(\frac{T_\lambda - T_P}{T_N - T_P}\right)^{\frac{1}{n}}, \tag{19}$$

which has to be equal to the heat flux through the He I phase q_I, defined as

$$q_I = -k_I \frac{T_\lambda - T_N}{(1-\gamma)\|\mathbf{d}\|}, \tag{20}$$

where k_I is the thermal conductivity of He I. Equating (19) and (20) yields

$$\frac{1-\gamma}{\gamma^{\frac{1}{n}}} = \frac{k_I}{q_{II,fict}\|\mathbf{d}\|}(T_N - T_\lambda)\left(\frac{T_N - T_P}{T_\lambda - T_P}\right)^{\frac{1}{n}}. \tag{21}$$

Eq. (21) is a nonlinear equation that can be solved numerically for the parameter γ. A simplified version of this approach was formulated by Noda et al. [34], who obtained an expression for $n = 3$ suitable for the finite difference method.

In order to correct the temperature gradient, it is useful to recall how the gradient field is computed numerically. The most popular method derives from a corollary of the Gauss theorem stating that the integral of the gradient of a scalar quantity ϕ over a volume V is equal to the surface integral of the flux through the closed surface S surrounding that volume:

$$\int_V \nabla\phi \mathrm{d}V = \oint_S \phi \mathrm{d}\mathbf{S}. \tag{22}$$

Eq. (22) can be numerically approximated as [35]:

$$(\nabla\phi)_P = \frac{1}{V_P}\sum_{f=1}^{N_f(P)} \phi_f \mathbf{S}_f, \tag{23}$$

where $N_f(P)$ refers to the total number of the faces of the control volume with centroid P. The value of the conserved quantity at the face center ϕ_f needs to be computed through linear interpolation between the centroid values of the cells sharing the face:

$$\phi_f = \lambda_f \phi_P + (1-\lambda_f)\phi_N, \tag{24}$$

where the coefficient λ is a geometric factor that determines the weight of the cell center values depending on the shape of the cells:

$$\lambda_f = \frac{S_{f,N}}{S_{f,N} + S_{f,P}}, \tag{25}$$

where the factors S_f are scalars defined as

$$S_{f,P} = \left\|\mathbf{S}_f \cdot \mathbf{C}_{Pf}\right\|, \tag{26a}$$

$$S_{f,N} = \left\|\mathbf{S}_f \cdot \mathbf{C}_{fN}\right\|. \tag{26b}$$

The vectors **C** represent the distance between the face center and the centroid of a cell.

From Eq. (23) it follows that the gradient calculation requires the value of the flux through the cell face. Eq. (24) tells us that the value of the temperature at the face center $T_{f,l}$ can be computed via linear interpolation between the center values of the cells sharing the face:

$$T_{f,l} = \lambda_{f,l} T_P + \left(1 - \lambda_{f,l}\right) T_N, \tag{27}$$

where the subscript l refers to the way the face center value is calculated (i.e., linearly interpolated), and the coefficient $\lambda_{f,l}$ is the geometric factor computed with Eq. (25). Therefore, the temperature at the face center has to be modified to properly calculate the flux. For this purpose, let us make a further adjustment to Eq. (21). Since the gradients use a linear interpolation scheme, the heat flux $q_{II,fict}$ can be computed as well as

$$q_{II,fict} = -k_{eff,fict} \frac{T_{f,l} - T_P}{\left\| \mathbf{C}_{Pf} \right\|}, \tag{28}$$

where $k_{eff,fict}$ is calculated using the temperature gradient before the application of the correction algorithm. Substituting Eq. (28) into (21) yields

$$\frac{1-\gamma}{\gamma^{\frac{1}{n}}} = \begin{cases} \frac{\left\|\mathbf{C}_{Pf}\right\|}{\|\mathbf{d}\|} \frac{k_l}{k_{eff,fict}} \frac{T_N - T_\lambda}{T_{f,l} - T_P} \left(\frac{T_N - T_P}{T_\lambda - T_P}\right)^{\frac{1}{n}}, & (a) \\ \quad \text{for } T_P < T_\lambda < T_N, & \\ \frac{\left\|\mathbf{C}_{fN}\right\|}{\|\mathbf{d}\|} \frac{k_l}{k_{eff,fict}} \frac{T_P - T_\lambda}{T_{f,l} - T_N} \left(\frac{T_N - T_P}{T_N - T_\lambda}\right)^{\frac{1}{n}}, & \\ \quad \text{for } T_N < T_\lambda < T_P. & (b) \end{cases} \tag{29}$$

Eq. (29a) refers to the case of the example in Fig. 1, whereas Eq. (29b) refers to the case in which the neighbor cell is in He II. These equations are solved iteratively using the Newton-Raphson method for nonlinear equations [36]. The coefficient γ ranges always between 0 and 1 for any value of the RHS of Eq. (29). The convergence of the Newton-Raphson method applied to Eq. (29) is always guaranteed for any value of the RHS and any arbitrary positive initial guess. The tolerance selected for the method is 10^{-5}, which is also chosen as the initial guess value. Moreover, due to the structure of Eq. (29), the method converges in few iterations regardless of the sought value of γ. These statements are demonstrated via calculus analysis, which can be found in Appendix A.

Once obtained γ, the exact location of the λ-front is known too, and it is possible to compute the corrected face center temperature. The idea consists in interpolating between temperature values within the liquid phase that crosses the face location, so that the numerical approximation involves just a region where the gradient is pretty much constant. Therefore, Eqs. (27) and (25) must be updated. For the case in which $T_P < T_\lambda < T_N$ (see Fig. 1), the updated factors S_f that determine the new λ_f read

$$S_{f,P} = \begin{cases} \left\| \mathbf{S}_f \cdot \mathbf{C}_{Pf} \right\|, & \text{for } \gamma \|\mathbf{d}\| > \left\| \mathbf{C}_{Pf} \right\|, \quad (a) \\ \left\| \mathbf{S}_f \cdot \left(\mathbf{C}_{Pf} - \gamma \mathbf{d}\right) \right\|, & \text{for } \gamma \|\mathbf{d}\| < \left\| \mathbf{C}_{Pf} \right\|, \quad (b) \end{cases} \tag{30}$$

and

$$S_{f,N} = \begin{cases} \left\| \mathbf{S}_f \cdot \left(\gamma \mathbf{d} - \mathbf{C}_{Pf}\right) \right\|, & \text{for } \gamma \|\mathbf{d}\| > \left\| \mathbf{C}_{Pf} \right\|, \quad (a) \\ \left\| \mathbf{S}_f \cdot \mathbf{C}_{fN} \right\|, & \text{for } \gamma \|\mathbf{d}\| < \left\| \mathbf{C}_{Pf} \right\|. \quad (b) \end{cases} \tag{31}$$

The face center temperature is finally computed as

$$T_f = \begin{cases} \lambda_f T_P + \left(1 - \lambda_f\right) T_\lambda, & \text{for } \gamma \|\mathbf{d}\| > \left| \mathbf{C}_{Pf} \right|, \quad (a) \\ \lambda_f T_\lambda + \left(1 - \lambda_f\right) T_N, & \text{for } \gamma \|\mathbf{d}\| < \left| \mathbf{C}_{Pf} \right|. \quad (b) \end{cases} \tag{32}$$

It is easily verifiable that, for $\gamma \|\mathbf{d}\|$ that tends to $\left\|\mathbf{C}_{Pf}\right\|$, T_f tends to T_λ from both sides of the face. Similarly it is done for the case in which $T_N < T_\lambda < T_P$. At last, the temperature gradient is updated using Eq. (23), and the He II properties (Eqs. (12) and (16)) are corrected accordingly.

3.1.2. Specific heat treatment

Another characteristic of the λ-transition is the discontinuity of the specific heat capacity at the λ-point. As known, the specific heat appears as part of the thermal diffusivity in the energy equation. The flux associated with the diffusion term in the energy equation requires the value of the diffusivity at the face shared by two adjacent cells. The face value is computed via linear interpolation between the cell centroids value. Let us consider again the case in Fig. 1. If the λ-front is located between the two cells, the interpolation of the specific heat at the face shared by those cells would result in an incorrect value due to the lambda discontinuity. Depending on the location of the front, interpolating between two values before and beyond the "λ" diverging peak may greatly underestimate the face value. Therefore, the specific heat interpolation must be corrected in those faces. Since these faces are the same ones treated in the previous subsection, the correction is simply achieved by using the algorithm presented before. Once the face temperature T_f (Eq. (32)) is updated, the specific heat is re-computed as a function of T_f.

Since the main variable in the energy equation herein presented is the enthalpy, the temperature must be derived consequently by means of the specific heat capacity. In OpenFOAM®, a Newton-based iterative algorithm is utilized for this purpose. However, the convergence of this method is strongly affected by the temperature dependence of the specific heat. In the case of He II, the algorithm diverges once T_λ is reached because of the specific heat discontinuity. Therefore, this algorithm was substituted with a method that interpolates values from an enthalpy-temperature table.

3.2. First-order phase transition

The first-order phase transition between subcooled He I and helium vapor is an ordinary phase change associated with vaporization/condensation. As such, it involves a latent heat of vaporization at the saturation point and interface phenomena due to high gradients in density across the two media. Various numerical models for multiphase phenomena are available in the literature. For compressible liquid/gas mixtures like in this case, one of the most popular groups of methods utilizes the Euler-Euler model [37], in which both the dispersed and continuous phases are considered as continua, and a phase fraction parameter determines the volume percentage occupied by each phase in a control volume. Many Euler-Euler solvers have been developed over the years. The most complex one is the two-phase model, which treats the phases separately and thus solves a distinct set of governing equations per phase. Due to this separation, additional terms describing the momentum transfer between the phases are needed. The two-phase model is typically chosen when the interaction surface between phases is very large, which usually happens for turbulent flows in macro-scale systems (e.g., bubble columns). In thin channels, as in the context of this study, the flow is mainly laminar and the dispersed phase is for the most part markedly separated from the continuous one [38]. Another type of Euler-Euler model is generally referred to as interface tracking method [39], which aims at resolving accurately the interface between the phases. Unlike the two-phase model, in this method, a single set of governing equations is solved for all the phases. The thermophysical and transport properties are averaged at each computational cell using the volume fraction of each phase. A separate transport equation for the volume fraction is solved at each iteration in order to advect the front and track its location. The interface tracking methods are commonly utilized for immiscible phases (e.g., water-air mixture), when the motion of the free surface is a key aspect.

For the simulations of this study, the helium mixture is treated as a whole and hence a single set of equations is solved. Since in this case the formation of helium vapor in a liquid helium chan-

nel is a result of a heat-driven phase change, the volume fraction is explicitly calculated from the mixture enthalpy and density instead of solving a transport equation, similarly to Voller's enthalpy method for fixed grids [40,41]. This allows circumventing the additional implicit partial differential equation for the volume fraction, thus decreasing the computational effort. This approach is possible owing to an energy equation expressed in terms of a state function (i.e., enthalpy) instead of temperature.

3.2.1. Thermophysical properties calculation

In isothermal problems, the common approach for the calculation of the thermophysical properties of a mixture consists of evaluating the portion of a volume occupied by a phase in order to weigh the property value among all the phases present in that volume. This requires the implicit solution of an additional transport equation to obtain the evolution of the mixture front over time. The problem under investigation, instead, involves unsteady thermodynamic conditions of the same fluid, which can be advantageously exploited to derive volume and mass fractions. Rather than tracking the front location, thus, *heliumChtFoam* computes explicitly the volume fraction α_I of the vapor-He I mixture as a function of the density:

$$\alpha_I = \min\left[\max\left(\frac{\rho-\rho_v}{\rho_l-\rho_v}, 0\right), 1\right], \tag{33}$$

where the subscripts v and l stand for the saturated conditions of vapor and liquid respectively. The total fluid density ρ is computed through the empirical compressibility factor Z:

$$\rho = \frac{p}{Z(h)RT}, \tag{34}$$

where R is the specific gas constant. The compressibility factor Z is extracted as a function of the enthalpy from the database HEPAK® [42], as all other properties. Since the two phases can coexist at saturation, α_I ranges from 0 (saturated vapor) to 1 (saturated liquid) depending on the vicinity to the saturated states. However, the total density of the fluid ρ does not always lie between the saturation values. The "min" and "max" functions are then necessary to ensure that α_I is bounded between physical quantities. The mass fraction Y_I is simply calculated as

$$Y_I = \min\left[\max\left(\frac{h-h_v}{h_l-h_v}, 0\right), 1\right]. \tag{35}$$

The temperature for $h_l \leq h \leq h_v$ is fixed to the saturation value T_{sat}.

The thermophysical properties at T_{sat} are weighed between the values at saturation as a function of α_I and Y_I. In particular, the transport properties (i.e., viscosity and thermal conductivity) are computed as

$$\mu_{sat} = \alpha_I \mu_l + (1-\alpha_I)\,\mu_v, \tag{36a}$$

$$k_{sat} = \alpha_I k_l + (1-\alpha_I)\,k_v, \tag{36b}$$

while the specific heat capacity as

$$c_{p,sat} = Y_I c_{p,l} + (1-Y_I)\,c_{p,v}. \tag{37}$$

Since α_I and Y_I are derived explicitly, the code is provided with pre-weighed properties that are interpolated at run time depending on the local enthalpy. At $T \neq T_{sat}$, the properties take the values corresponding to the only phase present in the control volume. The equivalent temperature steps chosen for the interpolating tables vary between 0.25 mK (nearby the λ-point) and 50 mK (far from the λ-point).

3.2.2. Surface tension

When a liquid is in contact with a gas, the liquid molecules at the interface are attracted by cohesion forces towards the bulk fluid. The adhesion force acting between molecules of a different phase is usually much lower than the cohesion force, leaving a net inward force that tends to contract the liquid. Because of the liquid contraction, a pressure jump arises across the interface. The surface, thus, experiences a tension force $\mathbf{F}_\sigma$ that is proportional to the pressure jump. In this work, the continuum surface force (CSF) model proposed by Brackbill et al. [43] is adopted for the calculation of $\mathbf{F}_\sigma$. Under the assumption of a constant surface tension coefficient σ, the CSF model estimates the pressure jump as

$$\Delta p = \sigma\kappa, \tag{38}$$

where κ is the curvature of the interface and is defined as the divergence of the interface unit normal vector:

$$\kappa = -\nabla\cdot\left(\frac{\nabla\alpha_I}{\|\nabla\alpha_I\|}\right). \tag{39}$$

The surface tension force is then

$$\mathbf{F}_\sigma = \frac{\rho}{\overline{\rho}_{sat}}\sigma\kappa\nabla\alpha_I, \tag{40}$$

where $\overline{\rho}_{sat}$ is the density averaged between the liquid and vapor saturation values. The condition $\mathbf{F}_\sigma \neq 0$ is satisfied just on the surface, where the volume fraction varies depending on the enthalpy. Moreover, the CSF model interprets the surface tension as a continuous volumetric force acting across the entire interface proportionally to the local total density. This proportionality allows thinning the interface without further numerical treatment of the front.

4. Boundary conditions

The peculiar physics of He II has impacts also on the conditions that must be set at the boundaries of a computational domain. In particular, two especially useful conditions pertain to the conjugate heat transfer at the interface with a solid part and the velocity of the fluid at the walls. These boundary conditions will be presented in the next subsections.

4.1. Kapitza heat transfer

When a heat flux is established through two different materials that are in contact, a thermal boundary resistance takes place between them. This resistance depends on the inverse of the temperature and hence it is usually negligible in the majority of the cases. In He II though, below the λ-point the temperature is low enough to make this resistance considerably important in the heat transfer mechanism between helium and a solid. This phenomenon results in a significant temperature jump across the solid-helium interface, which was first observed by Kapitza [44]. The heat exchange between the two media is strongly affected by the resulting Kapitza conductance h_K. The Kapitza conductance is dependent on the materials involved and their surface characteristics. For this reason, the temperature dependence of h_K is usually obtained experimentally for each material, and the resulting heat flux takes the form [45,8]

$$q = \begin{cases} a_{II} T_b^{m_{II}}\,(T_s - T_b), & \text{for } \Delta T \ll T, \quad \text{(a)} \\ a_I\left(T_s^{m_I} - T_b^{m_I}\right), & \text{for } \Delta T \approx T, \quad \text{(b)} \end{cases} \tag{41}$$

where a and m are empirical coefficients that depend on the solid material, T_b is the bath temperature of liquid helium, and T_s is the temperature of the solid surface.

Numerically, the thermal resistance can be imposed by considering a virtual layer between the He II and solid regions with a thermal resistance $1/h_K$. Equating the heat fluxes through the virtual layer and He II regions leads to the following temperature boundary condition for a generic computational cell with centroid P in the helium domain:

$$T_f = \frac{h_K C_{Pf}}{h_K C_{Pf} + k_{eff}} T_{f,nb} + \frac{k_{eff}}{h_K C_{Pf} + k_{eff}} T_P, \tag{42}$$

where $T_{f,nb}$ is the temperature at the interface between the solid and virtual layer regions, while the other parameters can be interpreted using Fig. 1 as a reference. The Kapitza conductance h_K is derived from Eq. (41) similarly to [46]:

$$h_K = \max\left(a_{II} T_b^{m_{II}}, a_I \frac{T_{f,nb}^{m_I} - T_b^{m_I}}{T_{f,nb} - T_b}\right). \tag{43}$$

The thermal behavior of the heater is described by the ordinary energy equation for solids:

$$\rho \frac{\partial h}{\partial t} = \rho \nabla \cdot (\beta \nabla h) + Q, \tag{44}$$

where β is the thermal diffusivity of the solid.

4.2. Superfluid slip

The common velocity boundary condition for an ordinary viscous fluid in contact with a wall is the no-slip condition, which simply sets the velocity of the fluid equal to zero. However, superfluid helium exhibits a wall slip behavior to a certain extent. From the theory of superfluid dynamics it emerges that, while the normal component of He II exerts a drag force on a solid body, the superfluid component moves with zero viscosity along the solid surfaces [47,48]. Indeed, as mentioned in Section 1, the superfluid component is inviscid and hence able to move tangentially to the walls. On the other hand, the normal component behaves like an ordinary fluid and remains static at the walls. This situation may be represented by a partial-slip condition of the total fluid [32]. The total fluid velocity at the walls is determined by imposing Eq. (9) equal to zero:

$$\mathbf{v}_\parallel = \frac{\rho_s}{\rho} M \nabla T_\parallel. \tag{45}$$

The velocity component $\mathbf{v}_\perp$ normal to the wall is obviously set to zero. The tangential component $\mathbf{v}_\parallel$ is obtained by removing the normal component from the temperature gradient:

$$\nabla T_\parallel = \nabla T - (\nabla T \cdot \mathbf{n})\mathbf{n}, \tag{46}$$

where $\mathbf{n}$ is the normal vector with respect to the wall. Eq. (45) is in agreement with the theory of He II, stating that the superfluid component is oppositely directed with respect to the heat flux. This can be verified by setting Eq. (3) to zero and substituting it into Eq. (4).

4.3. Superfluid boundary conditions in multiphase helium

Within the temperature range of helium vapor at ambient pressure, the fluid and solids are fully in thermal contact, and the Kapitza heat transfer mechanism is negligible. Furthermore, a viscous fluid without superfluid traits such as He I does not experience wall slip on solid surfaces. Nevertheless, the boundary conditions implemented in *heliumChtFoam* that are proper of He II do not require any modification due to the way they are formulated. More specifically, Eq. (43) allows the Kapitza resistance to fade away as the solid surface temperature gradually increases. This fade-out process starts when the Kapitza conductance for high differences in temperature (see Eq. (41b)) overcomes the one for low differences (see Eq. (41a)), which does not depend on the solid temperature. As the solid temperature increases because of the volumetric heat generation, the Kapitza resistance diminishes until the resulting temperature jump with helium is negligible. By the time the helium in contact with the heater turns into vapor, a perfect thermal contact between the two media is achieved.

The superfluid wall slip simply ceases to exist at T_λ, when the superfluid density becomes zero (see Eq. (45)) and hence a no-slip condition is imposed at the boundary. Moreover, the parameter M, which is also present in the superfluid slip equation, is automatically updated with the corrected temperature gradient field (see Sec. 3.1.1), resulting in the right value also at the boundaries where the λ-front intersects a wall. Consequently, the boundary conditions presented in this section adjust accordingly to represent the appropriate circumstances even in presence of phase changes.

5. Solution algorithm

The governing equations presented in Sec. 2 must be modified to account for multiphase phenomena. The continuity equation (Eq. (13)) remains essentially unchanged. The momentum equation (Eq. (11)) must include the surface tension force (Eq. (40)). Moreover, the parameter M must be updated with the corrected temperature gradient ∇T^* (see Sec. 3.1.1), where * identifies the corrected field. At T_λ, the superfluid terms in the momentum equation simply vanish as they all are proportional to the superfluid density, which becomes zero at the λ-transition. The energy equation (Eq. (14)) must comprise the conductive heat flux of He I and helium vapor too. Eq. (15) becomes then

$$\mathbf{q} = \frac{k_{He}}{c_p^*} \nabla h, \tag{47}$$

where c_p^* is the corrected specific heat capacity (see Sec. 3.1.2) and the thermal conductivity of helium k_{He} is defined as

$$k_{He} = \begin{cases} k_{eff}^*, & \text{for } T < T_\lambda, \quad \text{(a)} \\ k_I, & \text{for } T_\lambda \le T < T_{sat}, \quad \text{(b)} \\ k_{sat}, & \text{for } T = T_{sat}, \quad \text{(c)} \\ k_{vap}, & \text{for } T > T_{sat}, \quad \text{(d)} \end{cases} \tag{48}$$

where k_I and k_{vap} are the thermal conductivities of subcooled He I and superheated helium vapor respectively, whereas k_{sat} is computed with Eq. (36b). The effective thermal conductivity of He II k_{eff}^* is updated with the corrected temperature gradient field ∇T^* (see Sec. 3.1.1). The other thermophysical properties are set up similarly to Eq. (48).

The governing equations for multiphase helium are solved in a novel solution algorithm for transient conjugate heat transfer problems and compressible fluids in multidimensional domains. Fig. 2 represents the flow chart of *heliumChtFoam* with the modifications implemented for superfluid helium and its phase transitions with respect to the ordinary PIMPLE algorithm for compressible fluids [35]. The PIMPLE algorithm is an advanced version of the PISO (Pressure-Implicit with Splitting of Operators) algorithm, which is characterized by a single outer loop iteration. The solution algorithm starts by updating the current time and variables from the previous time step. The first outer loop iteration is then initiated by computing explicitly the superfluid and normal volume fractions. For the first iteration, the continuity equation is solved to compute the new density field. If the momentum predictor step is requested, the momentum equation is solved before the pressure correction loop. In the present work, the latter step is skipped as

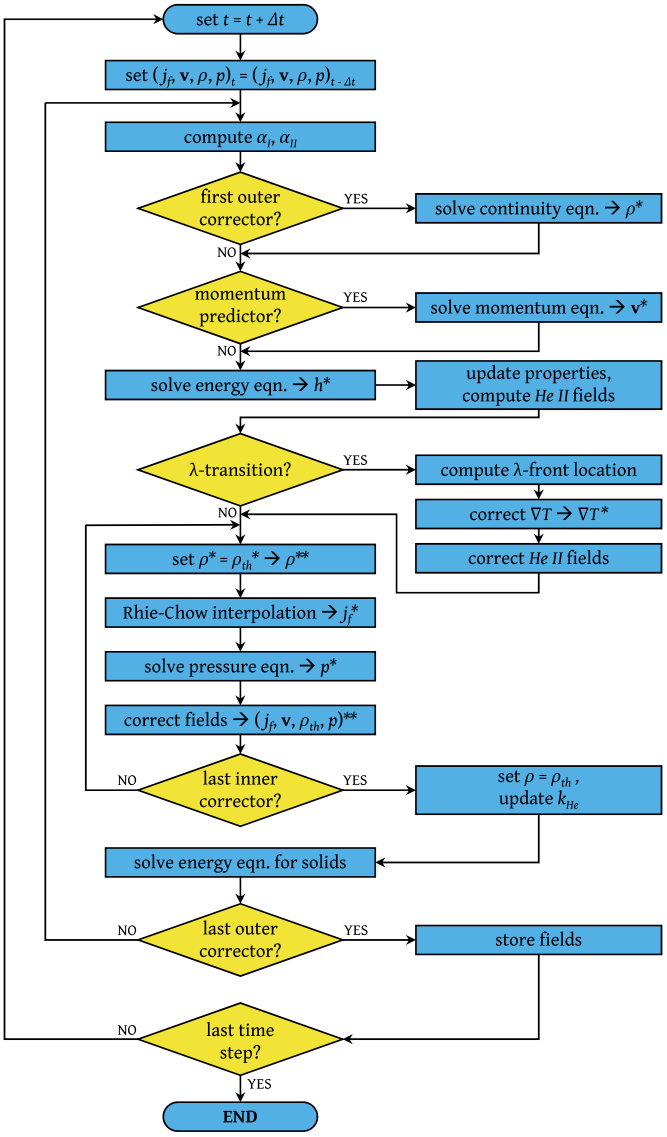

Fig. 2. *heliumChtFoam* PIMPLE algorithm. Single outer corrector in the case of PISO.

the physical phenomena involved are not advection-driven. The energy equation is then solved and the resulting enthalpy is used to update the thermophysical properties and superfluid helium parameters. At this point, if the temperature reaches the λ-point anywhere in the domain, the correction algorithm presented in Sec. 3.1.1 is activated in order to identify the exact location of the λ-front. As described previously, the front location is utilized to correct the temperature gradient and, consequently, the superfluid fields k^*_{eff} and M^*. If He II does not undergo the λ-transition, the correction algorithm is skipped and the inner loop is initiated. This loop is the classic pressure correction loop, where the pressure and momentum equations are solved iteratively until the attainment of velocity and pressure fields that satisfy the mass conservation. The subscript th in ρ_{th} serves to differentiate the thermodynamic density computed as a function of the enthalpy (Eq. (34)) from the one obtained by solving the continuity equation. After the last corrector iteration, the final density field is stored and the thermal conductivity field k_{He} is assembled. A diffusion equation (Eq. (44)) is then solved sequentially for each solid part present in the domain. The solution of the diffusion equations marks the end of an outer loop iteration, which, in the case of a PIMPLE algorithm, is repeated to facilitate the convergence stability and strengthen the coupling between fluids and solids. After the last outer loop, the fields are stored and the time marches forward. The whole sequence is repeated until the steady state.

6. Model validation

The severe non-linearity of the He II equations excludes the possibility to obtain analytical solutions for problems in which the impact of the temperature dependence of the properties is significant. For this reason, it was decided to validate *heliumChtFoam* against other models and data from both the literature and experiments conducted for this study. This section reports such comparisons for both He II and multiphase helium cases.

The simulations involving He II only were obtained through the PISO algorithm with three inner-loop iterations. For simulations involving solid parts or multiple phases, the PIMPLE algorithm (Fig. 2) was chosen instead. The setting comprises three inner-loop and ten outer-loop iterations to strengthen the coupling between the solid and helium solutions of the segregated algorithm and withstand the strong density variations associated with the first-order phase transition. The transient problem was solved using the Crank-Nicolson scheme with a blending factor of 0.9 [49]. Since this scheme may be unstable in certain problems, the blending factor increases its robustness by weighing the result with the pure implicit Euler scheme. As the following study cases are not advection-dominated, both the divergence and gradient terms were discretized with the central-difference scheme. The interpolated values between cell centroids were computed linearly. The linear systems of algebraic equations were solved with different methods depending on the unknown variable [49]: preconditioned conjugate gradient (PCG) method for the continuity equation; generalized geometric-algebraic multi-grid (GAMG) solver for the pressure equation; Gauss-Seidel for the momentum and energy equations. The solid diffusion equations were solved with the PCG method for symmetric matrices. The simulations were run in parallel utilizing 36 CPUs.

6.1. Single phase He II

The He II model was validated against data from both the benchmark steady-state experiment of Srinivasan and Hoffman [50] and a rectangular channel experiment conceived for this study. The comparisons of this sub-section regard He II only.

6.1.1. Srinivasan and Hoffman's tube experiment

Srinivasan and Hoffman conducted steady-state experiments in a 1 m long tube with an inner diameter of 3 mm. The He II is heated up at the center of the tube. The temperature is recorded at eight locations, which are 10 cm far from each other (starting at 10 cm from both sides of the tube). The tests that are within the interest of this study were carried out in stagnant conditions with a power deposition of 0.145 W and 0.205 W.

In order to compare *heliumChtFoam* to other models on equal terms, a one-dimensional uniform mesh constituted by 200 cells was chosen as the computational domain for this validation, in accordance with the simulations of Bottura and Rosso [31]. The time step was set to be adaptive such that the Courant–Friedrichs–Lewy number was always less than the unit. Since the experiment was originally conceived for forced flow tests, the apparatus was unable to maintain a stable temperature at the inlet and outlet of the tube at stagnant conditions. Therefore, it was decided to simulate only the region between the first and last sensors. Consequently, the temperature at the domain boundaries was set to the one measured by those sensors at the steady state. The initial temperature was assumed to be uniform in the whole domain and equal to the lowest boundary temperature. The pressure was fixed to the

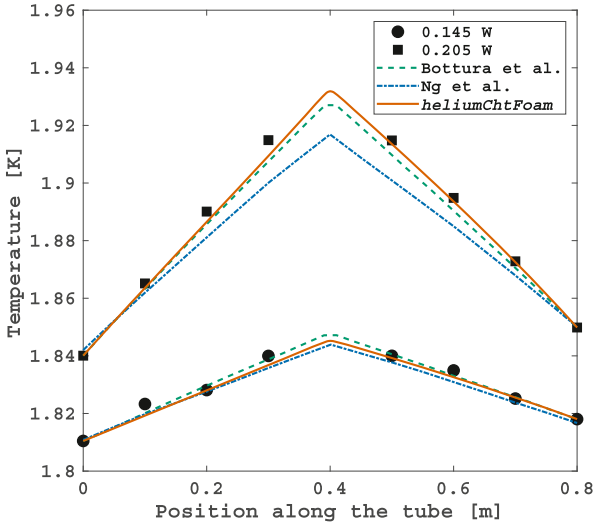

Fig. 3. He II temperature profiles comparison between *heliumChtFoam* (solid line) and data from Srinivasan and Hoffman's tube experiment (markers) [50]. The simulations by Bottura and Rosso [31], and Ng et al. [24] are also shown as dashed and dash-dotted line respectively.

experimental one (i.e., atmospheric pressure). Since the domain boundaries do not correspond to physical confines for the fluid, a possible backflow must be taken into account and hence two different conditions are imposed on the velocity depending on the flux direction: zero gradient if the flux points outward; pressure-dependent if the flux points inward. It is convenient to refer to this boundary condition as the inlet-outlet velocity condition from now on. The fluid was assumed to be initially static. The heat load was applied as a volumetric heat generation in the two central cells of the domain. The steady state was reached after 80 s and 150 s of simulated time for 0.205 W and 0.145 W respectively.

Fig. 3 shows the comparison between the computed temperature distribution along the tube by the present code and the data of the aforementioned experiments by Srinivasan and Hoffman [50]. The temperature profiles obtained by Bottura and Rosso [31], and Ng et al. [24] are also displayed in the figure. The set of governing equations of Bottura and Rosso's model is in terms of pressure, velocity, and temperature. They utilized a friction factor to model the viscous force, and the theoretical derivation of the heat conductivity function. Ng et al. used the classic two-fluid model with a double momentum equation. As it is clear from the figure, *heliumChtFoam* is in very good agreement with the experiments.

6.1.2. Rectangular cross-section channel experiment

The experimental setup consists of a rectangular cross-section channel of high aspect ratio [51]. The channel is 14 cm long, 5 cm wide, and 0.5 mm thick. The experiment was conducted at atmospheric pressure in a superfluid helium bath, where the channel setup was submerged. Since the free surface of the helium bath was only 40 cm above the channel location, the hydrostatic head was neglected in the simulations. One aperture of the channel is closed with a Manganin® heating strip as thick as the channel, while the opposite aperture is kept open to the bath (see Fig. 4). The channel is enclosed by thick stainless steel plates (i.e., 2 cm thick) that insulate thermally the He II contained in the channel from the bath. The steel plates were machined to ensure the smoothness of the surfaces in contact with helium. An insulating 2 cm thick G10 plug is situated behind the heater to achieve high thermal and electrical insulation for the heater. The relative position of all the pieces is fixed by several stainless steel screws covered with vacuum grease, which does not crack at cryogenic conditions. The vacuum grease is also inserted in the space between the plates to prevent superfluid leaks. The channel setup is equipped with nine bare chip Cernox® CX-1050-BC temperature sensors with a sapphire base for a fast thermal response. Eight of them are distanced 1.5 cm from each other along the centerline of the channel, and the closest sensor to the heater is 1.5 cm far from it. The farthest sensor from the heater is then 2 cm far from the aperture of the channel exposed to the bath. The ninth temperature sensor is situated behind the heater, inside the G10 plug. The channel was also equipped with two Kulite® cryogenic miniature ruggedized pressure transducers of the CTL-190 (M) series. These sensors revealed negligible pressure variations during the experiments, which justifies the assumption on the enthalpy definition in Eq. (15).

The experiment is a clamped heat flux test, in which the heater releases a constant heat load into the channel. The test was conducted at a bath temperature of 1.8 K and a 23.6 kW/m^2 heat flux. The computational geometry is a three-dimensional rectangular slab that resembles the shape of the channel filled with He II. The slab is subdivided into structured orthogonal uniform control volumes, which constitute a mesh of 27×10^3 cells (150 along the channel length and 36 along its width). The walls of the slab that correspond to the helium in contact with the stainless steel plates are kept adiabatic, while at the heater location the Neumann boundary condition is applied with the value of the heat flux. At the walls, the superfluid slip condition (see Sec. 4.2) is applied for the velocity, while the pressure gradient is velocity dependent and derived by inverting the semi-discretized momentum equation [52]. Since the latter pressure boundary condition is commonly used for walls, where the velocity is defined, it will be referred to as the fixed flux pressure condition from now on. The temperature and pressure at the open side of the channel are fixed to the bath one, while the velocity is computed through the inlet-outlet condition.

Fig. 5 shows the transient evolution of the temperature profile since the application of the clamped heat flux. The simulations agree satisfactorily to the data with a discrepancy of 0.38%, 0.21%, and 0.15% at 0.3 s, 0.7 s, and steady state respectively.

6.2. Phase transitions

As explained in Sec. 1, if the heat flux applied overcomes both the lambda and peak nucleate boiling heat fluxes, a helium triple-phase configuration establishes in the channel. This section reports the simulations of triple-phase phenomena in the experimental channel setup described in Sec. 6.1.2. Since the thermal time constant of helium vapor is comparable to the one of the components of the channel setup, it is essential for predicting the correct thermal behavior to include in the computation the solid parts surrounding the helium slab. However, considering the size of the steel plates with respect to the channel, a three-dimensional model of the setup would require a substantial computational effort. Therefore, despite the algorithm can be applied to three-dimensional problems, the phase change modules were tested in a two-dimensional domain that represents the cross-section of the setup at its centerline (i.e., 2.5 cm from the sides). The two-dimensional assumption is legitimized by the high aspect ratio of the channel.

6.2.1. Mesh tests

The mesh used for the simulations is a two-dimensional structured non-uniform grid with fully orthogonal control volumes. Since the mesh is fixed, it is of interest to investigate how the simulated steady-state location of the λ-front varies with the grid size. The domain created for these tests is shown in Fig. 6 with

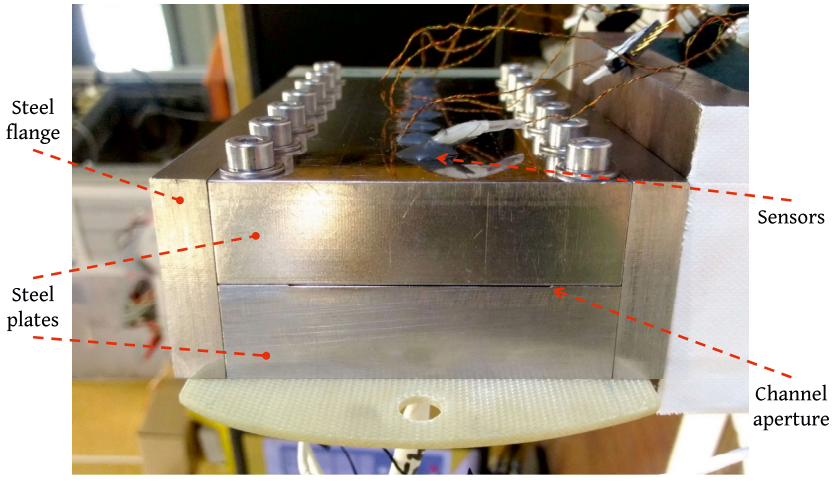

Fig. 4. Experimental channel setup.

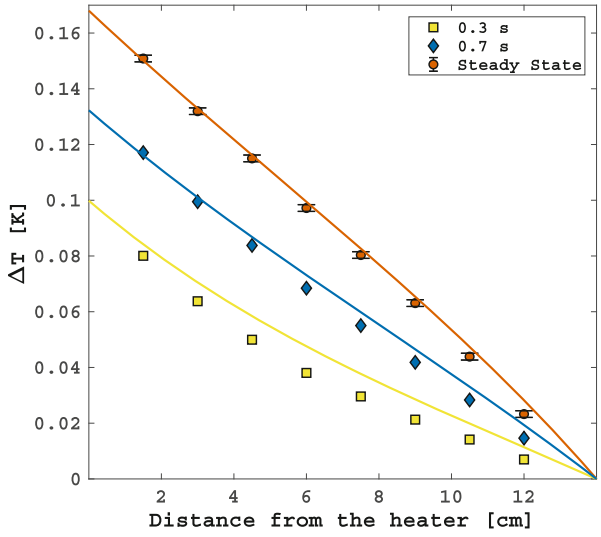

Fig. 5. Transient temperature profiles comparison between *heliumChtFoam* and data from an experiment in the horizontal 0.5 mm thick channel at a bath temperature $T_b = 1.8$ K and a heat flux $q = 23.6$ kW/m^2. The steady state is achieved after 8 s.

the real relative proportions of the sub-domains. The geometrical model includes both stainless steel plates, the G10 heater plug, the Manganin® heater, and the helium channel. The thermophysical properties of these materials were taken from CryoComp® [53]. The initial temperature of the entire system was set to 2.15 K, while the pressure of the fluid was set to the atmospheric one. As for the boundary conditions, at the walls the pressure is determined by the fixed flux condition, whereas the velocity is either computed through the superfluid slip condition for He II or zero for the other helium phases. The temperature at the bath and all external solid walls is fixed to the initial value. At the interfaces between helium and solids, the Kapitza condition is applied. Due to the lack of Kapitza resistance experimental data for the materials herein utilized, the empirical parameters were chosen similar to the as-received copper values [8]. As explained in Sec. 4.3, the Kapitza resistance tends naturally to zero as the temperature of the solid increases. Therefore, helium vapor results in perfect thermal contact with the solid. At relatively high heat fluxes, the Kapitza resistance between solids (e.g., heater and plug) is negligible [45], and hence neglected in this study. A volumetric heat generation was applied in the heater domain and equivalent to 5 kW/m^2 at the interface with the helium channel. An adaptive time step was used to ensure that the Courant number was always below the unit. The latter choice is particularly helpful in multiphase problems involving stagnant fluids as it shortens the time step only when needed, that is, in case a phase change associated with high variations in density occurs. In this case, a large time step is maintained as long as He II is the only fluid present in the channel. When vapor is generated, the significant density change causes a velocity increment, which shortens the time step to stabilize the computation.

With the exception of the heater, the grids of the solid components of the domain are all non-uniform with increasing cell size from the helium interface to the external boundaries, where the cells get as large as 5 mm for the steel plates and 2 mm for the G10 plug. Close to the helium slab, the cell size is 20 µm. The heater domain is constituted by uniform cells of around 23 µm. The channel thickness is subdivided into 11 cells, while the number of cells along its length is the varying parameter of this study. Four different grids were tested at the aforementioned conditions. Fig. 7 shows the cell size dependence of the λ-front position at the steady state as a normalized value with respect to the channel length. Despite the finest grid is forty times smaller than the coarsest one, the front position varies only within few percentage points, indicating that the correction algorithm for fixed grids (see Sec. 3.1.1) performs adequately. The slight non-monotonous behavior of the finest grid point is due to the small fluctuations of the λ-front because of the fluid motions.

The cell size chosen for the following simulations, which is indicated in Fig. 7, seemed to be a good compromise between accuracy and computational cost. To further decrease the numerical effort, it was decided to split the channel domain into two parts. The half next to the heater is discretized with the cell size chosen in this section, while the other half is non-uniform with increasing cell size towards the bath. Moreover, the channel thickness is split into 30 non-uniform cells. The final mesh is constituted by more than 67×10^3 hexahedra in the helium domain and more than 3×10^5 hexahedra in total with 5 degrees of freedom per computational cell.

6.2.2. Multi-region channel simulations

The simulations conducted for comparison with the experimental tests utilize a fixed temperature boundary condition at the interface between the G10 plug and the heater with the value measured at steady-state by the sensor installed in the plug (i.e., ninth sensor). As the thermal time constant of the heater is very low because of its size and thermal conductivity, fixing the temperature of the heater to its peak value since the beginning of the

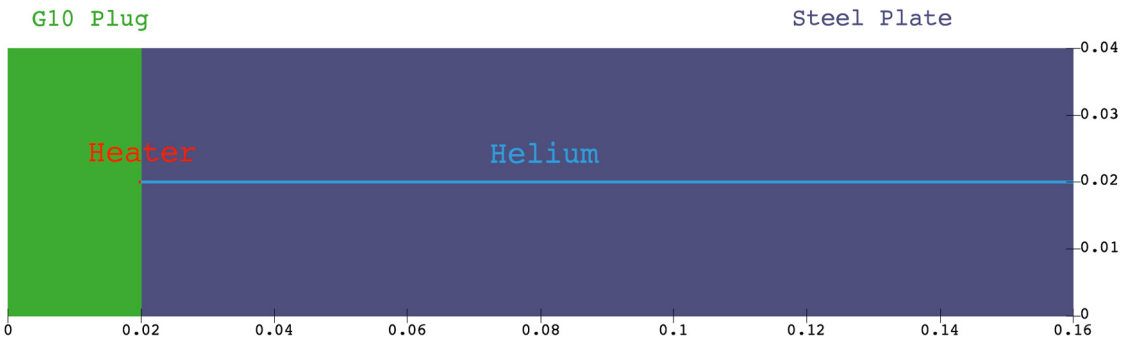

Fig. 6. Computational domain for the phase transitions simulations. The length coordinates are in meters.

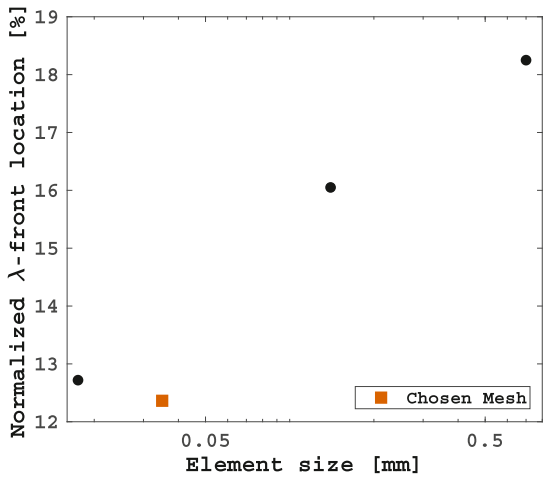

Fig. 7. Normalized λ-front position with respect to the channel length for grids of different cell longitudinal sizes.

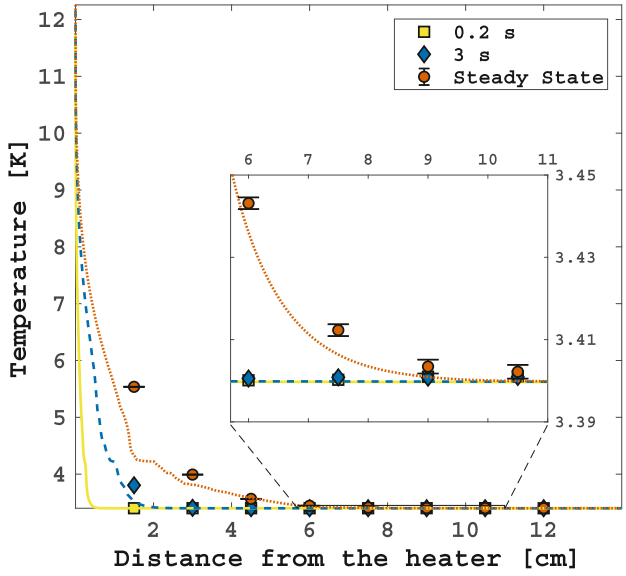

Fig. 8. Transient temperature profiles comparison between *heliumChtFoam* and data from an experiment in the downward vertical channel at a bath temperature $T_b =$ 3.4 K and the heater at 13.4 K.

transient is a reasonable assumption. The other boundary condition settings are the same as in Sec. 6.2.1.

Before simulating the double phase change, it is useful to focus at first on the first-order phase transition only. For this purpose, an experiment was conducted with the channel in vertical position with the helium bath above the λ-point. In this experiment, the

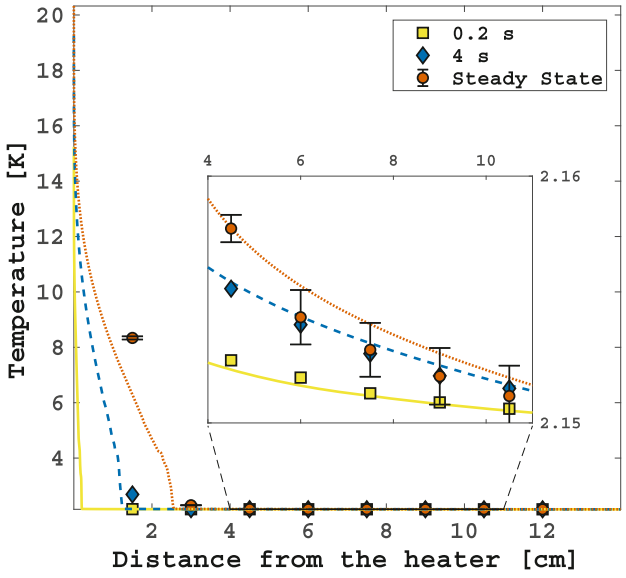

Fig. 9. Transient temperature profiles comparison between *heliumChtFoam* and data from an experiment in the downward vertical channel at a bath temperature $T_b =$ 2.15 K and the heater at 21.6 K.

heater, which is situated above the helium slab, reaches a temperature of 13.4 K, while the bath is maintained at 3.4 K. Fig. 8 shows the comparison between the simulated temperature profiles and data. The temperature rises sharply next to the heater and reaches almost instantaneously the peak value, which is slightly lower than the heater temperature for two reasons: the profile is probed along the interface with the steel plate that houses the sensors, where the temperature is less than the centerline of the channel; the fixed temperature is imposed behind the heater. The increase is so abrupt that any effect of the latent heat of vaporization is barely visible at the beginning of the transient. The boiling front advances slowly and, as it moves downstream, a plateau at the saturation temperature arises. Eventually, the front stops just below the location of the closest sensor to the heater. Although the temperature profile achieves the steady state after 50 s, the considerable gradient nearby the heater persists. The inset in Fig. 8 zooms in on the zone far from the heating surface, where the gradient is much lower. Although the simulated profile underestimates the temperature increment in helium vapor, it predicts satisfactorily the overall distribution with a relative error of 11.3 %.

A similar experiment was carried out in He II, with the bath at 2.15 K and the heater reaching 21.6 K at the steady state. The comparison with *heliumChtFoam* is displayed in Fig. 9. The temperature rises immediately above the saturation and lambda points. The resulting profiles share some features with the previous case. The temperature gradient is very high close to the heater, while it drops significantly beyond the λ-front. Both fronts develop slowly

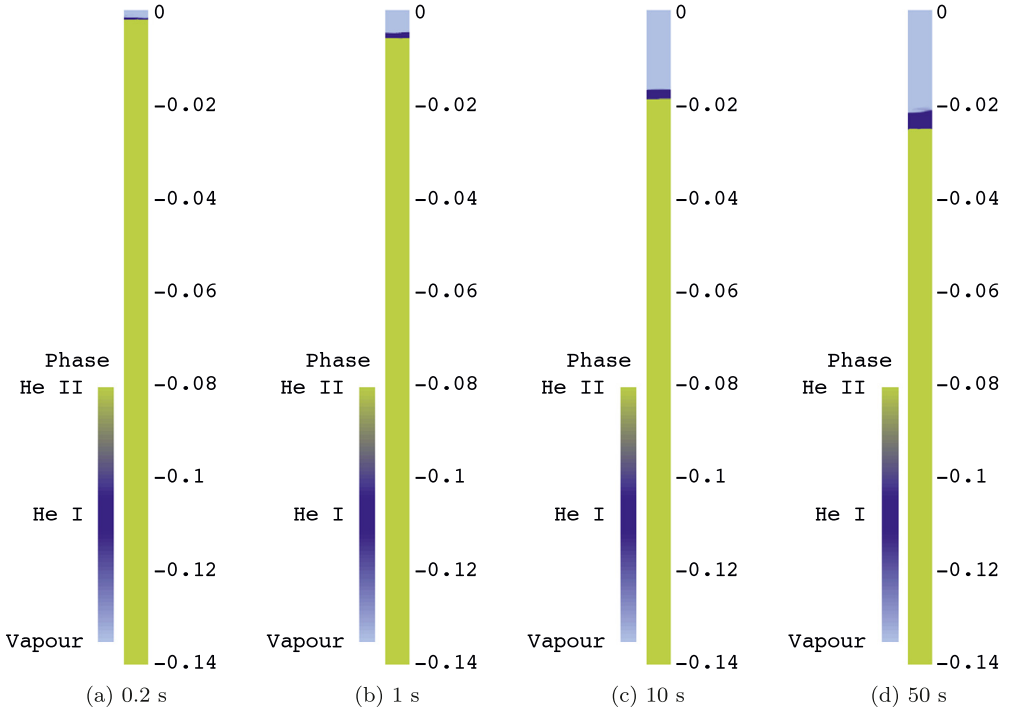

Fig. 10. Helium three-phase evolution in the downward vertical channel at a bath temperature $T_b = 2.15$ K and the heater at 21.6 K. The length coordinates are in meters.

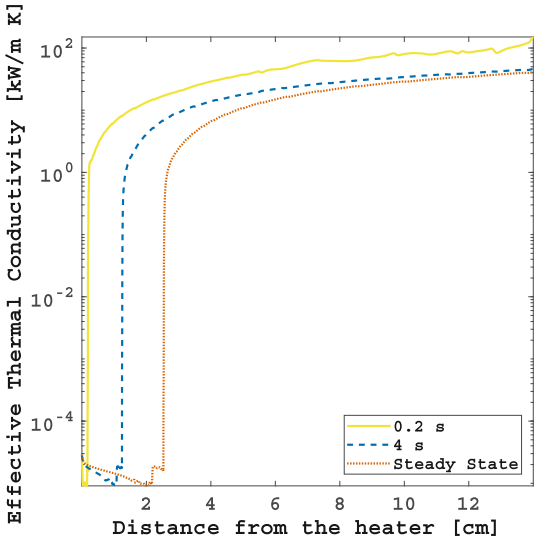

Fig. 11. Simulated thermal conductivity at the centerline of the downward vertical channel at a bath temperature $T_b = 2.15$ K and the heater at 21.6 K.

until a stable configuration is reached after 50 s. However, the plateau at the boiling point is almost absent in this case, indicating that the presence of the λ-front thins the boiling front. The inset shows a good agreement with the data downstream in the channel. The simulation underestimates once again the steady-state profile. Considering the temperature measured by the two closest sensors to the heater, the λ-front must lie between these sensors, indicating an acceptable estimation of its position by the model. Fig. 10 shows the volume fraction distribution in the channel at four moments of the simulation. The channel was magnified ten times in its thickness to favor a better visualization of the results in post-processing. It is clear how the vapor phase arises quickly at the beginning of the transient and expands downstream. The He I phase thickens in time but constitutes always a small portion of the channel between the vapor and He II phases. The fast onset of film boiling reduces the He II-He I transformation rate, limiting then the expansion of the He I phase. Fig. 11 shows the thermal conductivity (Eq. (48)) of the fluid in the same study case. The change of several orders of magnitude within the same substance is impressive and proper of the triple-phase phenomenon in helium. The value is maximum in He II next to the bath boundary, where the temperature gradient is minimum. It mildly decreases towards the λ-front, where the value drops significantly down to the He I range. Another small temperature reduction characterizes the phase change to helium vapor, where the minimum value is reached. The thermal conductivity of vapor increases towards the heater as a function of the temperature.

Another experiment in similar conditions was conducted with the channel in its horizontal orientation. In this case, the heater reaches a temperature of 22.7 K. Fig. 12 shows the comparison of the simulated temperature profiles with the data. The profiles are quite similar to the vertical orientation case, except the gradient is lower in vapor and He I. Since the lighter fluid phase is no longer gravity-driven towards the heater, the vapor expands further towards the bath. As a consequence, the λ-front propagates farther and exceeds the closest sensor to the heater at the steady state. As the inset shows, the profiles in He II are well predicted, particularly in the early moments of the test and despite the presence of the vapor phase. The overall temperature is slightly underestimated, with a satisfactory relative error of 7.9 %. This is more evident in Fig. 13, which shows the temperature evolution at the location of the three closest sensors to the heater. The simulated evolution is also in delay with respect to the data. However, the increase rate is well captured by the model. The underestimation might be due to the measured heater temperature, which may be lower than the actual one because of the location of the measurement. The volume fraction fields of this simulation are presented in Fig. 14, where the channel thickness is again magnified ten times. As in the previous case, the vapor is soon generated and grows slowly throughout the channel. However, the He I phase is visibly thicker than the vertical case. Another difference pertains to the shape of the boiling front, which appears tilted due to the effect of gravity. The same phenomenon is not observable, instead, for the λ-front,

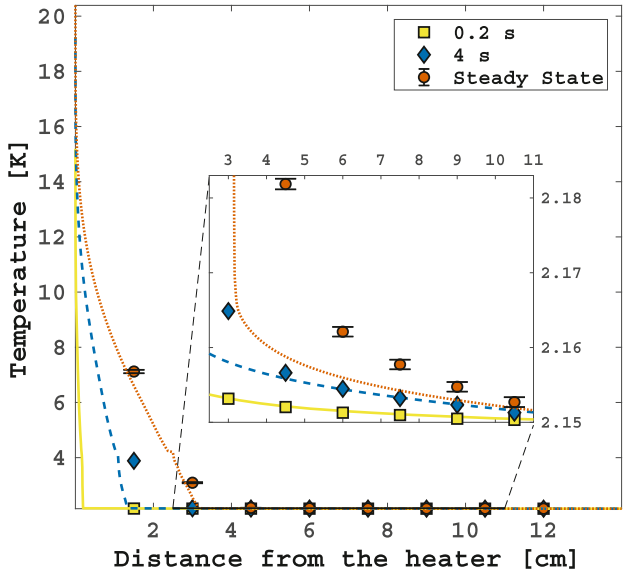

Fig. 12. Transient temperature profiles comparison between *heliumChtFoam* and data from an experiment in the horizontal channel at a bath temperature $T_b = 2.15$ K and the heater at 22.7 K.

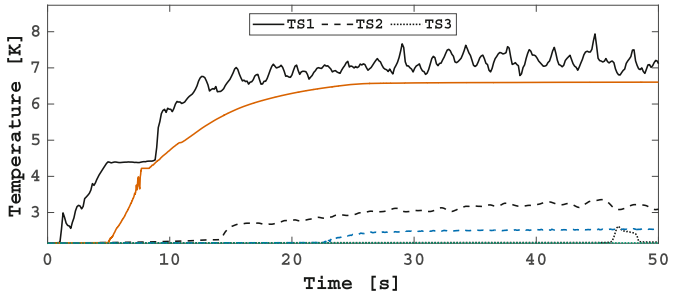

Fig. 13. Temperature evolution comparison between *heliumChtFoam* and data from the three closest sensors to the heater in the horizontal channel experiment at a bath temperature $T_b = 2.15$ K and the heater at 22.7 K. The distances between the heater and the sensors TS1, TS2, and TS3 are 1.5 cm, 3 cm, and 4.5 cm respectively. The linestyle of the simulation (colored) matches the measurement (black) for each sensor. (For interpretation of the colors in the figure(s), the reader is referred to the web version of this article.)

where the density gradient is very small and hence the interface is unaffected by buoyancy forces.

7. Conclusion

The following points summarize the conclusions of this study:

- A numerical model benchmarking validated a modified version of the single-fluid model for He II with a typical relative error of the transient temperature profiles below 1 %. This model, which is a FVM-based multidimensional code, comprises a generalized conductive heat power law, whose usage is extended to the momentum equation as well as the energy equation. The model includes also a customized superfluid partial slip boundary condition that captures the correct thermo-fluid dynamic behavior of He II at the walls.
- A segregated-like conjugate heat transfer module linked to the He II model enables simulating properly the thermal relationship between He II and solids through the usage of a customized Kapitza resistance boundary condition, which smoothly switches from a regime characterized by low helium-solid temperature differences to a regime where the temperature difference is comparable to the bath temperature.
- By combining the heat transfer equations of He I and He II, it is possible to derive a nonlinear equation for the λ-front position in fixed non-uniform orthogonal computational grids. The solution of this equation via the iterative Newton-Raphson method showed consistent and fast results.
- The comparison of data collected during He I experiments at moderate heat flux with a multiphase numerical model for boiling phenomena revealed good accuracy of the model with a relative error of the transient temperature profiles around 10 %. This model exploits the enthalpy dependence of the thermophysical properties to derive mass and volume fractions explicitly without tracking the vapor-He I interface. The model also implements a continuum surface force module for the calculation of the surface tension forces acting on the mixture interface.
- The comparison of data collected during He II experiments at moderate heat flux with a multiphase numerical model for triple-phase phenomena revealed good accuracy of the model with a relative error of the transient temperature profiles around 10 %. The model is based on a modified PIMPLE algorithm, which includes the module for the identification of the λ-front location. This additional module allows to correct at the λ-front the He II fields that depend on the temperature gradient. The predicted λ-front position varies weakly with the size of the control volumes.
- The triple-phase numerical model simulates satisfactorily the propagation of the phase change fronts. The channel portion occupied by the He I phase resembles the one observed in the experiments of the non-confined channel. The simulations revealed that the saturation interface between vapor and He I is thinner if boiling occurs in an environment initially constituted by He II only.

Nomenclature

Romans letters

$\mathbf{C}$	distance vector between cell centroid and face, m
$\mathbf{d}$	distance vector, m
$\mathbf{F}_\sigma$	surface tension force, N m^{-3}
$\mathbf{g}$	gravitational acceleration vector, m s^{-2}
$\mathbf{n}$	normal vector, m
$\mathbf{q}$	heat flux vector, W m^{-2}
$\mathbf{S}$	surface normal vector, m^2
$\mathbf{v}$	velocity vector, m s^{-1}
a	empirical coefficient, -
A_{GM}	Gorter-Mellink coefficient, m s kg^{-1}
c	specific heat capacity, J kg^{-1} K^{-1}
f	heat conductivity function, m^5 K W^{-3}
h	specific enthalpy, J kg^{-1}
h_K	Kapitza conductance, W m^{-2} K^{-1}
j	mass flux, kg s^{-1} m^{-2}
K	kinetic energy, J kg^{-1}
k	thermal conductivity, W m^{-1} K^{-1}
M	momentum diffusive-like parameter of superfluid helium, m^2 s^{-1} K^{-1}
N	number of cell faces, -
n	conductive heat power law coefficient, -
p	pressure, Pa
Q	source/sink function, -
q	heat flux, W m^{-2}
R	specific gas constant, J K^{-1} mol^{-1}
S	surface scalar, m^2
s	specific entropy, J kg^{-1} K^{-1}
T	temperature, K
t	time, s

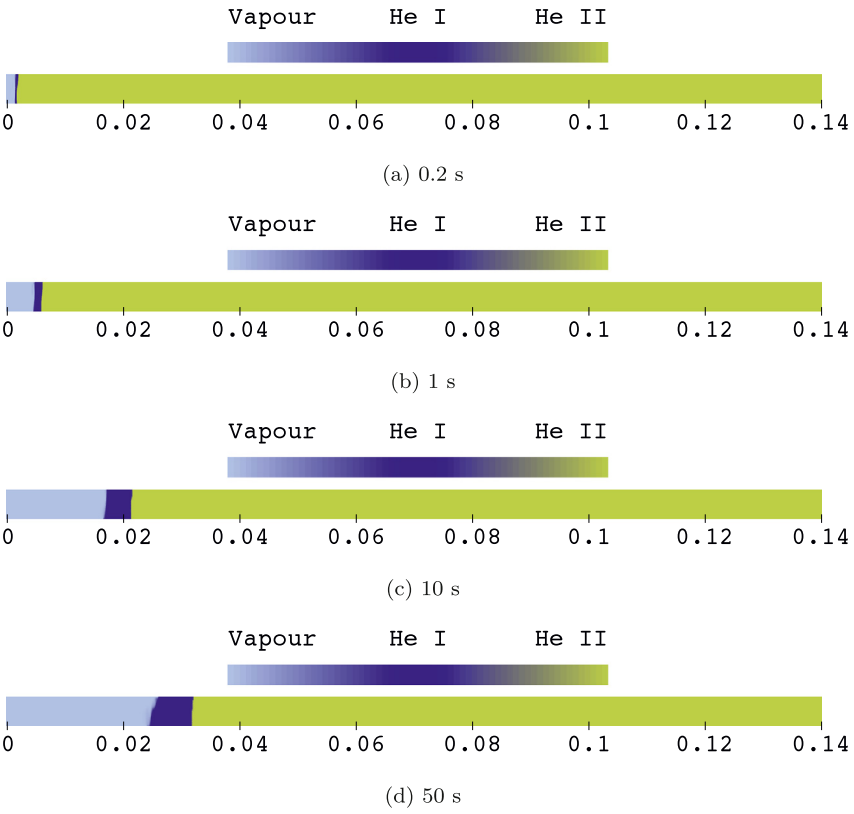

(a) 0.2 s

(b) 1 s

(c) 10 s

(d) 50 s

Fig. 14. Helium three-phase evolution in the horizontal channel at a bath temperature $T_b = 2.15$ K and the heater at 22.7 K. The length coordinates are in meters.

V	volume, m^3
v	velocity, m s^{-1}
x	position coordinate, m
Y	mass fraction, -
Z	compressibility factor, -

Greek letters

α	volume fraction, -
β	thermal diffusivity, m^2 s^{-1}
γ	weighing coefficient, -
κ	interface curvature, m^{-1}
λ	geometric factor, -
μ	dynamic viscosity, Pa s
ϕ	scalar quantity, -
ρ	density, kg m^{-3}
σ	surface tension coefficient, N m^{-1}

Superscripts

$*$	new iteration, corrected

Subscripts

λ	lambda point, lambda transition related
b	bath
eff	effective
f	cell face
$fict$	fictitious
He	helium
I	reference to He I
II	reference to He II
l	saturated liquid, linearly interpolated
N	neighbor cell centroid
n	normal fluid component
ns	relative or mutual action between the two fluid components
P	owner cell centroid
p	constant pressure
s	superfluid component, solid surface
sat	saturation conditions
v	saturated vapor
vap	superheated vapor

Acronyms

CSF	Continuum Surface Force
FVM	Finite Volume Method
LHS	Left-Hand Side
RHS	Right-Hand Side

Declaration of competing interest

The authors declare that they have no known competing financial interests or personal relationships that could have appeared to influence the work reported in this paper.

Acknowledgement

This research was mainly supported by EASITrain – European Advanced Superconductivity Innovation and Training. This Marie Skłodowska-Curie Action (MSCA) Innovative Training Networks

(ITN) received funding from the European Union's H2020 Framework Programme under grant agreement no. 764879. The authors would like to thank the CERN CryoLab and Rob Van Weelderen for proposing and supporting forward-looking experiments through a CERN-CEA collaboration. The authors are grateful to Vadim Stepanov (CEA-Saclay) for the precious technical support during the experiments and Will Bainbridge (CFD Direct Ltd) for the invaluable suggestions on numerical methods.

Appendix A. Correction algorithm analysis

It is interesting to make a few considerations about the applicability and efficiency of the Newton-Raphson method to this particular problem. Since all the parameters on the RHS of Eqs. (29a) and (29b) are known at each time step, let us group them into a coefficient B, which is always non-negative. Let us consider then the following function:

$$f(\gamma) = B\gamma^{\frac{1}{n}} + \gamma - 1. \tag{A.1}$$

We are interested in finding the root γ_0 of $f(\gamma)$, which will be the result of the nonlinear equation. The Newton-Raphson method searches for the roots of a given function by iteratively computing its tangent at a spot that is closer to the root at each iteration. The convergence of this method strongly depends on the initial guess value. For example, the presence of an inflection point between the guess value and the root might make the method diverge. Therefore, it is important to choose a proper guess value γ_g that ensures convergence regardless of the location of the λ-front and hence the value of B. Let us first calculate the first derivative of $f(\gamma)$:

$$f'(\gamma) = \frac{\mathrm{d}f(\gamma)}{\mathrm{d}\gamma} = 1 + \frac{B}{n}\gamma^{\frac{1-n}{n}}. \tag{A.2}$$

Thus, $f'(\gamma)$ is always positive for any B, which means that $f(\gamma)$ has no stationary point, and that the minimum and maximum possible values of γ_0 can be determined through the following limits:

$$\lim_{B\to 0}\left[f(\gamma)=0\right] \quad \Rightarrow \quad \gamma_0 = 1, \tag{A.3a}$$

$$\lim_{B\to +\infty}\left[f(\gamma)=0\right] \quad \Rightarrow \quad \lim_{B\to +\infty}\left[\gamma^{\frac{1}{n}} + \frac{\gamma}{B} - \frac{1}{B} = 0\right] \quad \Rightarrow \quad \gamma_0 = 0. \tag{A.3b}$$

As initially expected, the values of γ_0 range from 0 to 1 for any B.

In the Newton-Raphson method, the new guess value $\gamma_{g,new}$ is calculated at each iteration as follows:

$$\gamma_{g,new} = \gamma_g - \frac{f(\gamma_g)}{f'(\gamma_g)}. \tag{A.4}$$

When the difference between $\gamma_{g,new}$ and γ_g is below a pre-defined tolerance tol, the loop is stopped. Because of the degree of Eq. (A.1), γ_g has to be always non-negative for $f(\gamma_g)$ to be computed numerically. Moreover, for γ_g that tends to 0, $f'(\gamma)$ tends to infinite, giving rise to a floating point error. This means that $\gamma_{g,new}$ at each iteration has to be always positive:

$$\gamma_{g,new} > 0 \quad \Rightarrow \quad \gamma_g < \left[\frac{n}{(n-1)\,B}\right]^n. \tag{A.5}$$

For B tending to infinite, γ_g tends to 0, which means that above a certain value B_{tol} such that

$$f(tol) = 0 \quad \Rightarrow \quad B_{tol} = \frac{1 - tol}{tol^{\frac{1}{n}}}, \tag{A.6}$$

γ_g will be less than the tolerance value, making the loop pointless. Therefore, for $B \geq B_{tol}$, γ_0 is set to tol. When $B < B_{tol}$, if tol is also used as the initial value for γ_g, then Eq. (A.5) requires that

$$tol < \left[\frac{n}{(n-1)\,B}\right]^n \quad \Rightarrow \quad B_{max} = \frac{n}{(n-1)\,tol^{\frac{1}{n}}}, \tag{A.7}$$

where B_{max} is the maximum value of B that allows the use of tol as initial value for γ_g. It is thus necessary that $B_{tol} \leq B_{max}$, which imposes the following condition on tol:

$$tol \geq \frac{1}{1-n}. \tag{A.8}$$

Since n is either equal to 3 or 3.4, Eq. (A.8) is always met regardless of the desired order of accuracy for the algorithm.

The inequality (A.5) sets a condition on the initial guess value to properly initiate the loop. However, this is not enough to ensure the convergence of the algorithm. In order to check so, let us calculate the second derivative of $f(\gamma)$ as

$$f''(\gamma) = \frac{\mathrm{d}^2 f(\gamma)}{\mathrm{d}\gamma^2} = \frac{B\,(1-n)}{n^2}\gamma^{\frac{1-2n}{n}}. \tag{A.9}$$

Considering the possible values of n, it is clear that $f''(\gamma)$ is always non-positive. This means that $f''(\gamma)$ never changes sign and hence $f(\gamma)$ has no inflection point. Therefore, as long as the condition in (A.5) is satisfied, the loop will surely converge to the root.

As a last consideration, it is useful to qualitatively estimate the convergence speed of the algorithm depending on the value of γ_0. Let us analyze how the first guess $\gamma_g = tol$ could affect the number of iterations needed to reach convergence through the following limits:

$$\lim_{B\to B_{tol}}\left[f(\gamma)=0\right] \quad \Rightarrow \quad \gamma_0 \simeq \gamma_g, \tag{A.10a}$$

$$\lim_{B\to 0}\left[f'(\gamma)\right] \quad \Rightarrow \quad f'(\gamma) = 1. \tag{A.10b}$$

The limit (A.10a) indicates that the greater B, the closer the root to the initial guess. Whereas the second limit implies that for B tending to small values, the tangent of the curve tends to a constant value, pointing immediately to an area nearby the root. Therefore, in the limiting cases, the convergence seems to be facilitated.

Appendix B. Supplementary material

Supplementary material related to this article can be found online at https://doi.org/10.1016/j.cpc.2021.108275.

References

[1] P. Lebrun, L. Serio, L. Tavian, R. Weelderen, in: P. Kittel (Ed.), Advances in Cryogenic Engineering, Vol. 43, Springer, US, 1998, pp. 419–426.
[2] B. Baudouy, M. François, F.-P. Juster, C. Meuris, Cryogenics 40 (2) (2000) 127–136.
[3] C.E. Chase, Phys. Rev. 127 (2) (1962) 361–370.
[4] G. Ahlers, Phys. Rev. Lett. 22 (2) (1969) 54–56.
[5] P. Leiderer, F. Pobell, Z. Phys. A, Hadrons Nucl. 223 (4) (1969) 378–384.
[6] G. Bon Mardion, G. Claudet, P. Seyfert, Cryogenics 19 (1) (1979) 45–47.
[7] A. Sato, M. Maeda, Y. Kamioka, in: Proceedings of the Twentieth International Cryogenic Engineering Conference (ICEC20), Elsevier, 2005, pp. 849–852.
[8] S.W. Van Sciver, Helium Cryogenics, Springer, New York, 2012.
[9] S. Caspi, T. Frederking, Cryogenics 19 (9) (1979) 513–516.
[10] S. Breon, S. Van Sciver, Cryogenics 26 (12) (1986) 682–691.
[11] P. Ehrenfest, Phasenumwandlungen im ueblichen und erweiterten Sinn, classifiziert nach den entsprechenden Singularitaeten des thermodynamischen Potentiales, N. V. Noord-Hollandsche Uitgevers Maatschappij, 1933.
[12] K. Hama, M. Shiotsu, Cryogenics 47 (4) (2007) 209–219.
[13] T. Noda, N. Fujimoto, Y.F. Rao, K. Fukuda, in: Proceeding of International Heat Transfer Conference 11, Begellhouse, 1998, pp. 219–224.
[14] T. Okamura, T. Suzuki, N. Seki, S. Kabashima, Cryogenics 34 (3) (1994) 187–193.

[15] S. Mao, C.A. Luongo, D.A. Kopriva, Int. J. Heat Mass Transf. 49 (25) (2006) 4786–4794.
[16] H.G. Weller, G. Tabor, H. Jasak, C. Fureby, Comput. Phys. 12 (6) (1998) 620–631.
[17] L. Tisza, Nature 141 (3577) (1938) 913.
[18] F. London, Phys. Rev. 54 (11) (1938) 947–954.
[19] L.D. Landau, Phys. Rev. 60 (4) (1941) 356–358.
[20] R. Feynman, Chapter II Application of Quantum Mechanics to Liquid Helium, Progress in Low Temperature Physics, vol. 1, Elsevier, 1955, pp. 17–53.
[21] C. Gorter, J. Mellink, Physica 15 (3) (1949) 285–304.
[22] H.E. Hall, W.F. Vinen, Proc. R. Soc. Lond. Ser. A, Math. Phys. Sci. 238 (1213) (1956) 215–234.
[23] I.L. Bekarevich, I.M. Khalatnikov, J. Exp. Theor. Phys. 13 (1961) 643.
[24] Y.S. Ng, J.H. Lee, W.F. Brooks, J. Thermophys. Heat Transf. 3 (2) (1989) 203–212.
[25] V.F. Rao, K. Fukuda, H. Horie, Cryogenics 36 (6) (1996) 457–464.
[26] K. Takamatsu, N. Fujimoto, Y. Rao, K. Fukuda, Cryogenics 37 (12) (1997) 829–835.
[27] H. Tatsumoto, K. Fukuda, M. Shiotsu, Cryogenics 42 (1) (2002) 19–28.
[28] C. Soulaine, M. Quintard, H. Allain, B. Baudouy, R. Van Weelderen, Comput. Phys. Commun. 187 (2015) 20–28.
[29] A. Kashani, S.W. Van Sciver, J.C. Strikwerda, Numer. Heat Transf., Part A, Appl. 16 (2) (1989) 213–228.
[30] N. Ramadan, R. Witt, Cryogenics 34 (7) (1994) 563–577.
[31] L. Bottura, C. Rosso, Int. J. Numer. Methods Fluids 30 (8) (1999) 1091–1108.
[32] T. Kitamura, K. Shiramizu, N. Fujimoto, Y. Rao, K. Fukuda, Cryogenics 37 (1) (1997) 1–9.
[33] C. Hirsch, Numerical Computation of Internal and External Flows: Fundamentals of Computational Fluid Dynamics, Elsevier/Butterworth-Heinemann, 2007.
[34] T. Noda, Y. Rao, N. Fujimoto, K. Morita, K. Fukuda, Technol. Rep. Kyushu Univ. 73 (2000) 53–61 (in japanese).
[35] F. Moukalled, L. Mangani, M. Darwish, The Finite Volume Method in Computational Fluid Dynamics: An Advanced Introduction with OpenFOAM® and Matlab®, Springer International Publishing, 2016.
[36] A. Quarteroni, F. Saleri, P. Gervasio, Scientific Computing with MATLAB® and Octave®, Springer, 2014.
[37] M. Ishii, T. Hibiki, Thermo-Fluid Dynamics of Two-Phase Flow, Springer, 2011.
[38] M. Wörner, Microfluid. Nanofluid. 12 (6) (2012) 841–886.
[39] J.M. Hyman, Physica D 12 (1) (1984) 396–407.
[40] V. Voller, C. Prakash, Int. J. Heat Mass Transf. 30 (8) (1987) 1709–1719.
[41] V.R. Voller, C.R. Swaminathan, B.G. Thomas, Int. J. Numer. Methods Eng. 30 (4) (1990) 875–898.
[42] HEPAK®, version 3.4, Cryodata Inc., P.O. Box 173, Louisvile, CO 80027.
[43] J. Brackbill, D. Kothe, C. Zemach, J. Comput. Phys. 100 (2) (1992) 335–354.
[44] P.L. Kapitza, Phys. Rev. 60 (4) (1941) 354–355.
[45] E.T. Swartz, R.O. Pohl, Rev. Mod. Phys. 61 (3) (1989) 605–668.
[46] M.B. Gorbounov, L. Bottura, J.R. Miller, S.W. Van Sciver, Finite Element Code for Quench and Stability Analysis of Superconducting Magnets Cooled by He II, Advances in Cryogenic Engineering, vol. 41, Springer US, 1996, pp. 335–342.
[47] L.D. Landau, E.M. Lifshitz, Fluid Mechanics, Pergamon Press; Addison-Wesley Pub. Co., 1959.
[48] S.J. Putterman, Superfluid Hydrodynamics, North-Holland Pub. Co.; American Elsevier Pub. Co, 1974.
[49] J.H. Ferziger, M. Perić, Computational Methods for Fluid Dynamics, Springer, Berlin Heidelberg, 2002.
[50] R. Srinivasan, A. Hofmann, Cryogenics 25 (11) (1985) 641–651.
[51] A. Vitrano, R. Bruce, B. Baudouy, IOP Conf. Ser., Mater. Sci. Eng. 755 (2020) 012068.
[52] M. Darwish, F. Moukalled, Numer. Heat Transf., Part B, Fundam. 37 (1) (2000) 103–139.
[53] CryoComp®, version 5.3, Eckels Engineering Inc., Florence, SC 29501-8006.